

Research Article

A Novel Space Large Deployable Paraboloid Structure with Power and Communication Integration

Tao Zheng , Zheng Fei, Xi Rui, and Lide Yan

Department of Electronic Mechanism, School of Mechano-Electronic Engineering, Xidian University, Xi'an, Shaanxi 710071, China

Correspondence should be addressed to Tao Zheng; taozheng@stu.xidian.edu.cn

Received 21 May 2019; Revised 21 October 2019; Accepted 25 October 2019; Published 13 November 2019

Academic Editor: Raffaele Solimene

Copyright © 2019 Tao Zheng et al. This is an open access article distributed under the Creative Commons Attribution License, which permits unrestricted use, distribution, and reproduction in any medium, provided the original work is properly cited.

The combination of a solar array and a communication antenna can reduce the entire mass, physical size, and cost in space applications. Currently, related studies mainly focus on the combination of the two structures on the one flat plate structure (FPS). Compared with the FPS, a paraboloid structure has a lower surface density and higher conversion efficiency. Therefore, a novel space large deployable paraboloid structure with power and communication integration (SSPCI) is proposed and designed in detail, for spacecraft on a sun synchronous earth orbit; it consists of a cable mesh membrane reflector (CMMR), an energy conversion device (ECD), and a three-extensible-rod (TER) pointing mechanism. To achieve the goal of integrating power and communication, the TER pointing mechanism drives the CMMR/ECD to track the sun in the sunshine region or to turn to face the ground station/other target in the Earth's shadow region. Then, through simulation analyses of the deploying process, static force at a limit orientation, and sun tracking process of the SSPCI, it is proved that the SSPCI is feasible and has satisfactory performance. Finally, deploying experiments of the folded hoop of the CMMR and sun tracking experiments of the TER pointing mechanism on the ground were carried out successfully, which proves that the folded hoop can be deployed successfully with fairly high deploying dependability, and the TER pointing mechanism is feasible for the SSPCI from the mechanism principle and the control mode in space applications indirectly. Moreover, the tracking accuracy of the TER pointing mechanism is estimated to be within $\pm 0.4^\circ$ although the machining precision of its components is not high.

1. Introduction

As limitations of size of rockets carrying and cost of launching, it is a challenging issue to reduce the mass, physical size, and cost of major spacecraft components in space applications [1]. Generally, most spacecraft include at least one large-size solar array to provide power and one large-size communication antenna to establish a high gain and robust communication with the ground station. Both the two structures require a massive and large back support to maintain their surface tolerance. Moreover, they may interfere with each other in space. One solution to reduce the burden of these two large structures on the spacecraft is to combine them into one.

Currently, related research mainly focuses on the combination of a solar array and a communication antenna on the one flat plate structure (FPS). One technical scheme is

to arrange the solar array and communication antenna on the same side of the FPS, and the other is to arrange them on different sides of the FPS.

For the first technical scheme, two ideas are proposed according to the arrangement sequence of the solar array and communication antenna. One idea is to arrange the communication antenna in front of the solar array, and the other is to use the opposite arrangement. For the first idea, researchers carry out several feasible structures. Two antennas integrating with solar arrays are designed by Huang and Zawadzki for space vehicle applications [2]. In both antenna designs, the printed microstrip radiator, because of its small size and low profile, is selected as the element for the antenna array to be integrated with the solar array. A novel hybrid technology is presented by Vaccaro et al., where amorphous silicon solar cells are either integrated or physically combined with printed slot antennas [3]. Meshed

patch antennas are directly integrated onto the solar cells of a small satellite to save valuable surface real estate that are proposed by Turpin and Baktur [4]. O’Conchubhair et al. studied the effect of a solar cell lattice on the performance of an IFA antenna [5]. An et al. designed, manufactured, and tested a Ka band reflectarray antenna integrated with solar cells, where solar cells are used as the reflectarray antenna substrate [6]. Because the communication antenna is on the front of the solar array, although the antenna has satisfactory radiation characteristics, an optical blockage for sunlight must exist in this structure. For the second idea, related research is less than the one of the first idea. Vaccaro et al. presented a new antenna which combines solar cells and printed patches. It is designed so as to accommodate the solar cells which provide power to a monolithic microwave integrated circuit amplifier [7]. Solar cells are on the top of this antenna. Similarly, solar cells may affect radiation characteristics of the antenna because the solar array is on the front of the communication antenna.

For the second technical scheme, it is easier to implement than the first one. Huang proposes the back of the microstrip reflectarray can be used for solar arrays [8]. Holland et al. proposed an origami style solar/antenna panel where the phased array is located on the opposite side of the solar array [9]. Compared with the first technical scheme, this scheme is applied in the case where sunlight and electromagnetic waves incident the spacecraft from both sides.

As mentioned above, although a solar array and a communication antenna could be integrated on one FPS, they will interact with each other when arranged on the same side of a FPS. Furthermore, the surface density of an integrated FPS is high, and its conversion efficiency is low. Compared with the FPS, a paraboloid structure has a lower surface density and higher conversion efficiency because it focuses sunlight or electromagnetic waves at the focal point. However, there are few studies on a paraboloid structure with power and communication integration. Only Lichodziejewski and Cassapakis have developed a power antenna concept, utilizing an inflatable membrane paraboloid reflector to concentrate solar energy for space electrical power generation, while concurrently or alternatively acting as an antenna with large aperture and high gain [10]. This power antenna is used for spacecraft on a deep space exploration orbit (DSEO), where sunlight and electromagnetic waves irradiate the spacecraft continuously from the same side. By adjusting the attitude of the spacecraft, this power antenna can concurrently receive sunlight and electromagnetic waves.

A sun synchronous earth orbit (SSEO), where the sun and earth are on both sides of a spacecraft, respectively, is different from a DSEO. Therefore, sunlight and electromagnetic waves irradiate a spacecraft on a SSEO from different sides, respectively. Most spacecraft on the SSEO need more power and higher communication capacity than those on the DSEO. However, a paraboloid structure with power and communication integration for spacecraft on the SSEO has never been studied.

For this purpose, a novel space large deployable paraboloid structure with power and communication integration (SSPCI) for spacecraft on the SSEO is proposed in this paper, as shown in Figure 1. Section 2 of this paper presents a novel

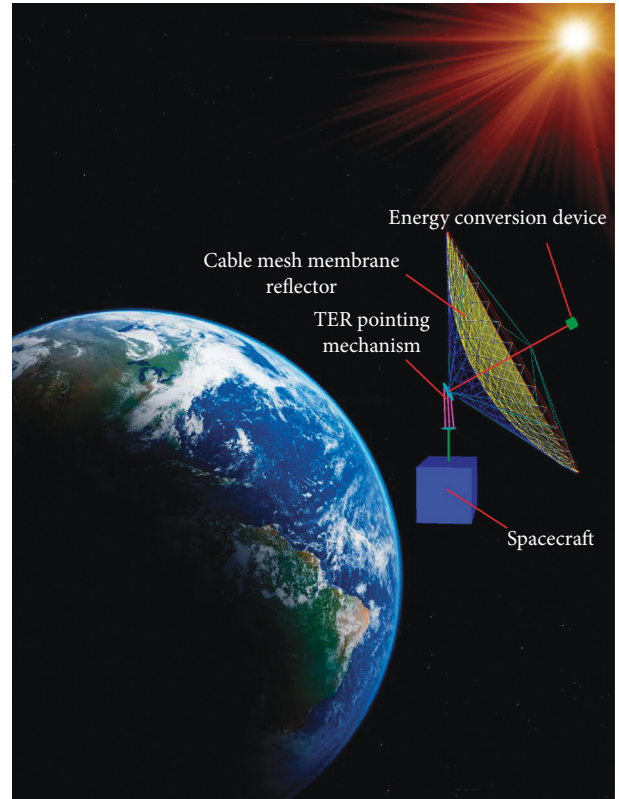


FIGURE 1: Schematic of the SSPCI.

idea for integrating power and communication for the SSPCI, and then the overall structural design of the SSPCI is described, which consists of a cable mesh membrane reflector (CMMR), an energy conversion device (ECD), and a TER pointing mechanism for driving the CMMR/ECD to track the sun for power in the sunlight region or to turn to face the ground station for communication or achieving other targets in the earth shadow region. Following this, the key components of the SSPCI are structurally designed in Section 3. The tracking principle is deduced and elaborated for the SSPCI in Section 4. The simulation analyses of deploying process, static force, and sun tracking process of the SSPCI are addressed in Section 5. Deploying experiments of the CMMR and sun tracking experiments of the TER pointing mechanism on the ground were carried out successfully, as described in Section 6. Finally, Section 7 concludes the work with a summary.

2. Description of Space Large Deployable Paraboloid Structure with Power and Communication Integration

As is known, spacecraft on the SSEO always spend part of their time in the sunshine region and part of their time in the earth shadow region in a flight cycle. Based on this, a novel idea for integrating power and communication is proposed: when spacecraft are in the sunshine region, the SSPCI loaded on it tracks the sun for power; when spacecraft are in the earth shadow region, the SSPCI turns to face the ground station for communication or achieving other targets.

Based on this idea and our research on space large deployable antennas [11–13], the overall structure of the SSPCI is proposed, as shown in Figure 2. The SSPCI consists of a CMMR, a TER pointing mechanism, and an ECD. From the perspective of the whole system structure, the SSPCI has a simple and efficient structure, and each component is itself a mature structure. Therefore, the system has high stability and reliability.

2.1. Consideration of Cable Mesh Membrane Reflector and Energy Conversion Device. For the reflector of the SSPCI, an ultralight CMMR is proposed, as shown in Figure 2. It uses a folded hoop and a central cylinder as its rigid backbone; flexible cables are used with them to form a mesh surface on which the aluminized membrane is assembled. The aluminized membrane can reflect both sunlight and electromagnetic waves. Meanwhile, a preliminary physical model of the CMMR is shown in Figure 3.

The ECD is fixed to the focal point of the CMMR by the central cylinder. A beam splitter or metallic grid is mounted in front of a solar cell array or lightweight thermoelectric conversion device [14] and is used to reflect electromagnetic waves onto a feed, as shown in Figure 2 [10]. In this way, sunlight and electromagnetic waves can be separated and utilized for power or communication.

2.2. Design of Three-Extensible-Rod (TER) Pointing Mechanism. The TER pointing mechanism is the most key component of the SSPCI which is used to drive the CMMR/ECD to track the sun or to turn to face the ground station/other target. Before proceeding with design, the mounting position of the SSPCI on the spacecraft should be determined firstly.

Most spacecraft on the SSEO adopt three-axis attitude stabilization, and their body coordinate system (BCS) and orbital coordinate system (OCS) coincide to implement ground orientation easily. The sun's path on the OCS is a spiral shape when a spacecraft is travelling on the SSEO. It can be treated as a circle in one cycle. According to the mounting position of solar arrays on a spacecraft and the position relationship between the sun and the earth's center relative to a spacecraft, a mounting position for the SSPCI is determined. For example, for a hexahedron spacecraft, the SSPCI is mounted at the center of the plane of the spacecraft that is parallel to the orbital plane and faces towards the sun, as shown in Figure 4. Not only can the SSPCI satisfy the requirements of sun tracking but also it can easily turn to face the ground station for communication or achieving other targets at this position.

After the mounting position has been determined for the SSPCI, a TER pointing mechanism is proposed, as shown in Figure 5. The TER pointing mechanism includes a base platform, a mobile platform, and three extensible rods. Three extensible rods, all with the same structure, are arranged between the two platforms in an equilateral triangle. The lower end of each extensible rod is connected to the base platform by a rotary joint, and the upper end is connected to the mobile platform by a compound joint. Huang and Zeng

point out that the TER pointing mechanism has three degrees of freedom, two rotational motions, and an independent vertical translational motion [15]. The two rotational motions can satisfy the requirement of the SSPCI, while the independent vertical translational motion can be used to pull the mobile platform down to the base platform to reduce the carrying size of the TER pointing mechanism in the rocket fairing. The TER pointing mechanism is simple and lightweight in structure. It has high tracking accuracy, low inertia, and a fast response speed [16].

2.3. Achievement of Integrating Power and Communication. As shown in Figure 2, the SSPCI is connected to the spacecraft by a supporting rod; a rotary joint is at the lower end of the supporting rod where a motor is equipped for the deployment of the SSPCI, and the upper end of the supporting rod is fixed to the base platform of the TER pointing mechanism. The mobile platform is connected to the lower end of the central cylinder of the CMMR by a rotary joint on which a motor is equipped for the deployment of the SSPCI. When the SSPCI is tracking the sun for power, the length of three extensible rods are controlled to allow the mobile platform to rotate along axis Y_b in BCS $O_b - X_b Y_b Z_b$. When the SSPCI needs to turn to face the ground station, the TER pointing mechanism keeps the elevation angle in the process of tracking the sun unchanged and rotates along axis Y_b back to the direction of axis Z_b , while the SSPCI rotates around the rotary joint at the lower end of the supporting rod until the central cylinder points towards the center of the earth, as shown in Figure 6.

3. Structural Design of Key Components of SSPCI

3.1. Deployable Joint of CMMR. The deployable joint, which is used to connect and drive the folded hoop to deploy in place, is the most key structure of the CMMR. The joint with a pair of synchronize gears, which is driven by torsion springs, is a fair satisfactory selection for a space large deployable structure [17]. Figure 7 shows the physical model of the deployable joint. Simplified taper gears are used to drive rods of the hoop from the horizontal position to vertical position. When the folded hoop is folded, the stretch energy is stored in torsion springs. Clamps and pins are used to connect the parts of the joint together. The deployable joint is simple and lightweight in structure, which has a fairly high deploying dependability.

3.2. Compound Joint of TER Pointing Mechanism. For tracking the sun, the TER pointing mechanism needs to implement a large range motion. Instead of a spherical joint, a smart compound joint with a hook joint and rotary joint is used to connect each extensible rod with the mobile platform, whose axes converge at one point, as shown in Figure 8; its rotation range is theoretically $\pm 180^\circ$. Compared with the spherical joint, this smart compound joint can increase the workspace of the TER pointing mechanism and

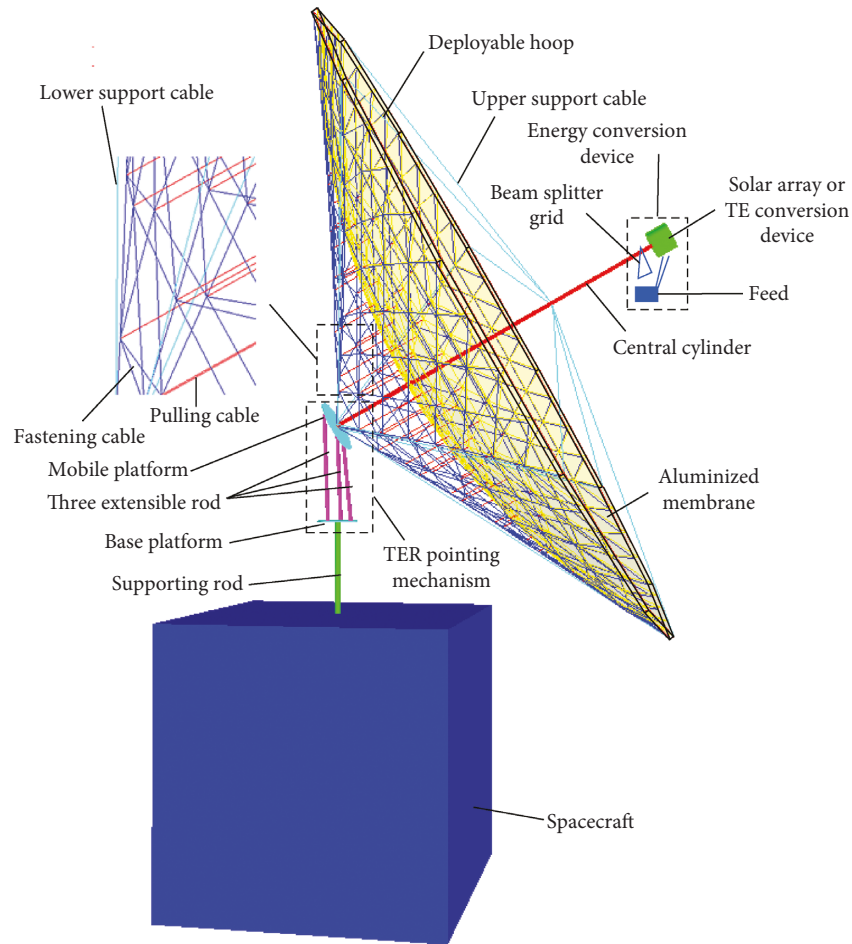


FIGURE 2: Overall structural design of the SSPCI.



FIGURE 3: Preliminary physical model of the CMMR.

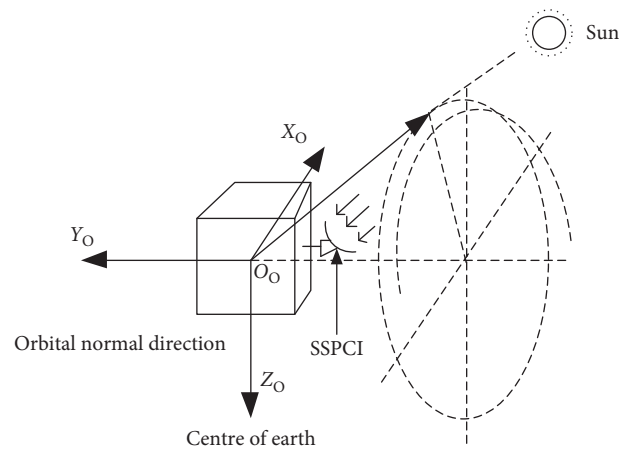


FIGURE 4: Determination of the mounting position.

reduce the difficulty of manufacturing. An exploded diagram of the compound joint is shown in Figure 9.

4. Motion Control of TER Pointing Mechanism

4.1. Inverse Kinematic Analysis of TER Pointing Mechanism. Figure 10 presents the kinematic model of the TER pointing mechanism. First, a static coordinate system, $O - XYZ$, is

established at center O of the base platform where axis Z is vertically upward along the base platform, axis X points towards the center point of rotary joint (R) R_1 at the lower end of extensible rod 1, and axis Y is formed as the cross-product of the two previous axes (right-hand rule is applied). A mobile coordinate system, $o - xyz$, is established at center o of the mobile platform; axis z is vertically upward along the

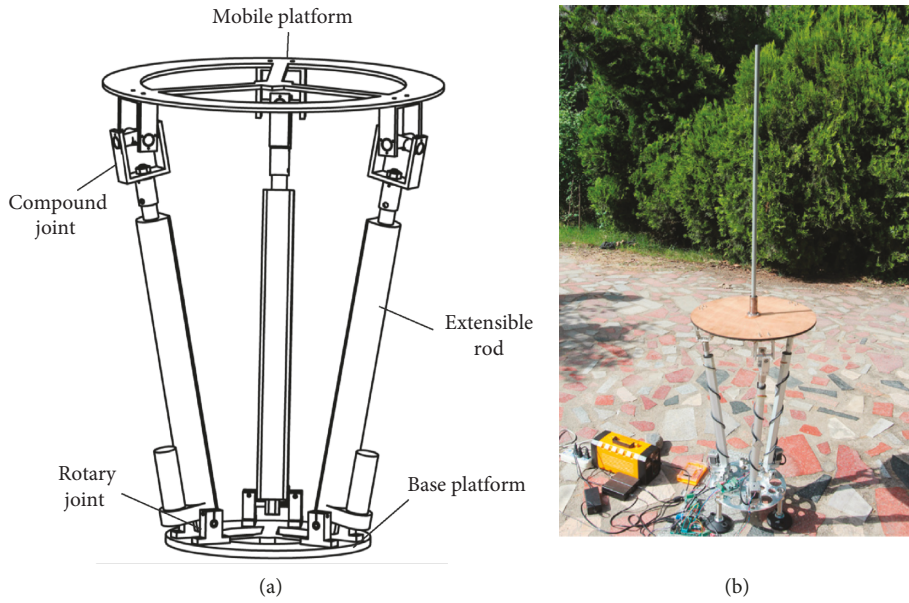


FIGURE 5: Structure of the TER pointing mechanism: (a) diagram; (b) physical model.

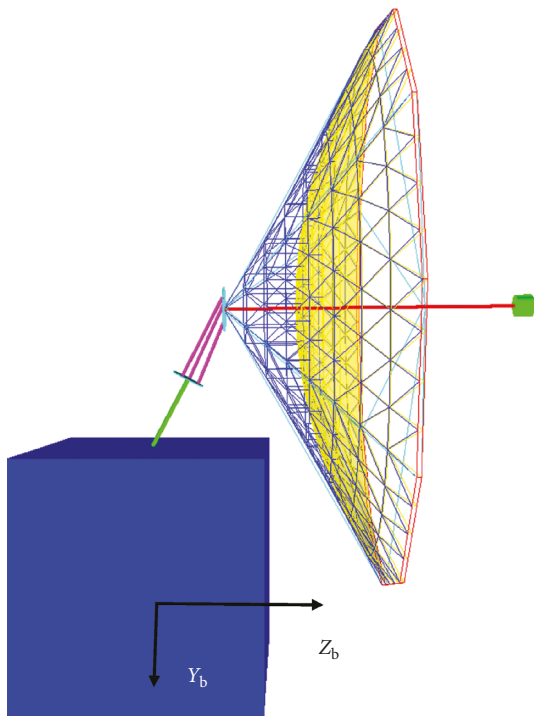


FIGURE 6: Status of the SSPCI for communication.



FIGURE 7: Physical model of the deployable joint.

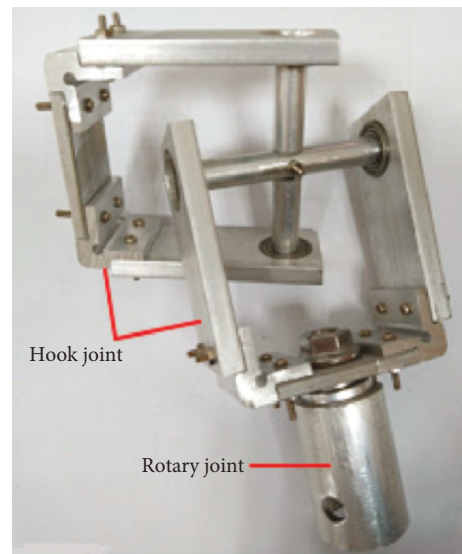


FIGURE 8: Structure of the smart compound joint.

mobile platform, axis x points towards the center of the compound joint, S_1 , at the upper end of extensible rod 1, and axis y is formed as the cross-product of the two previous axes (right-hand rule is applied). r is the radius of the mobile platform, and R is the radius of the base platform. In addition, the mobile platform is connected to the lower end of the central cylinder of the CMMR by a rotary joint (R) at its center point R_4 , which rotates along axis y .

The position and orientation of the TER pointing mechanism can be expressed as

$$W = W(\alpha, \beta, \gamma, x, y, z), \quad (1)$$

where x , y , and z denote the position coordinate of the center of the mobile platform in $O - XYZ$; α , β , and γ , named, the Z - Y - Z Euler angle, are used to describe the

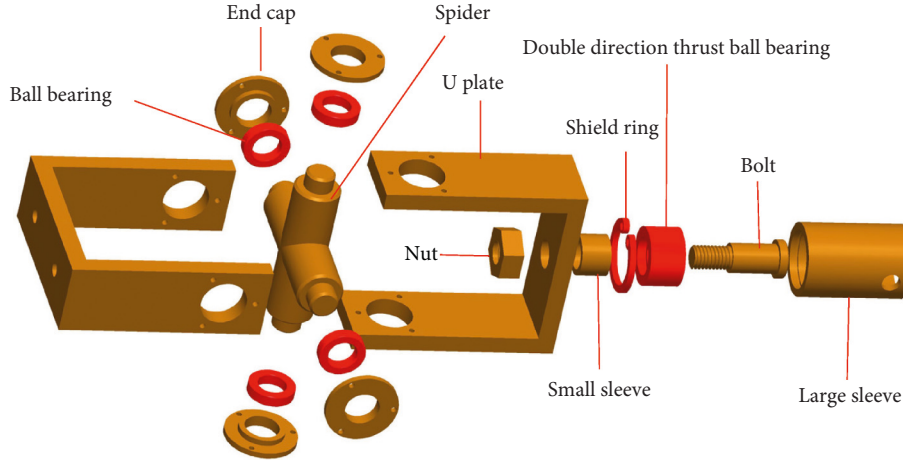


FIGURE 9: An exploded diagram of the smart compound joint.

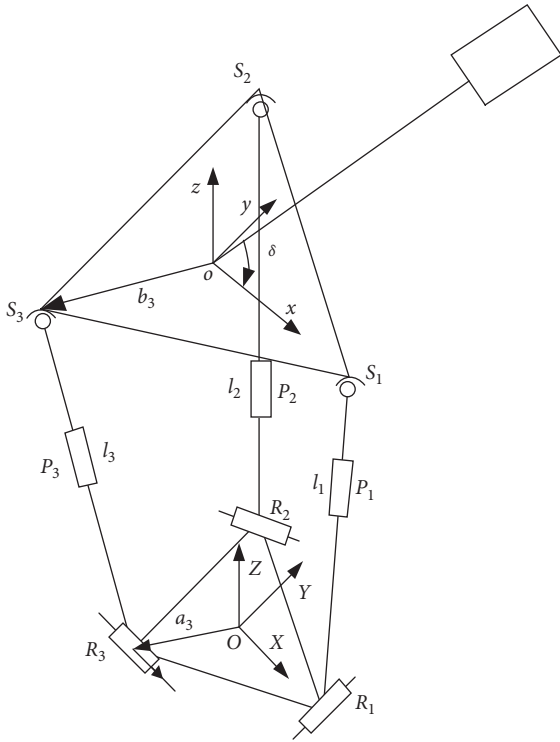


FIGURE 10: Geometry of the TER pointing mechanism.

orientation of the mobile platform relative to the base platform. The homogeneous transformation matrix from $o - xyz$ to $O - XYZ$ is

$$T = \begin{bmatrix} cac\beta c\gamma - sas\gamma & -cac\beta s\gamma - sac\gamma & cas\beta & x \\ sac\beta c\gamma + cas\gamma & -sac\beta s\gamma + cac\gamma & sas\beta & y \\ -s\beta c\gamma & s\beta s\gamma & c\beta & z \\ 0 & 0 & 0 & 1 \end{bmatrix}, \quad (2)$$

where c and s denote \cos and \sin , respectively.

According to the structure constraint of the TER pointing mechanism, x , y , and z can be represented by other parameters as follows:

$$\begin{cases} x = \frac{r \cos 2\alpha (\cos \beta - 1)}{2}, \\ y = \frac{r \sin 2\alpha (1 - \cos \beta)}{2}, \\ \gamma = -\alpha. \end{cases} \quad (3)$$

Let $a_i = \overrightarrow{OR_i}$ in $O - XYZ$ and $b_i = \overrightarrow{oS_i}$ in $o - xyz$. Then, the vector of each extensible rod in $O - XYZ$, L_i , can be expressed as

$$L_i = T(\alpha, \beta, \gamma, x, y, z) \begin{bmatrix} b_i \\ 1 \end{bmatrix} - \begin{bmatrix} a_i \\ 1 \end{bmatrix}, \quad i = 1, 2, 3. \quad (4)$$

Substituting equation (3) in equation (4), L_i is described as

$$L_i = T(\alpha, \beta, z) \begin{bmatrix} b_i \\ 1 \end{bmatrix} - \begin{bmatrix} a_i \\ 1 \end{bmatrix}, \quad i = 1, 2, 3. \quad (5)$$

Carrying out a modular operation to two ends of equation (5) yields

$$l_i = \|L_i\| = \left\| T(\alpha, \beta, z) \begin{bmatrix} b_i \\ 1 \end{bmatrix} - \begin{bmatrix} a_i \\ 1 \end{bmatrix} \right\|, \quad i = 1, 2, 3. \quad (6)$$

4.2. For Sun Tracking. As mentioned above, the BCS $O_b - X_b Y_b Z_b$ and OCS $O_o - X_o Y_o Z_o$ of the spacecraft on the SSEO coincide to implement ground orientation easily. According to VSOP (variation seculaires des orbits planetaires) 87 theory [18, 19], the unit direction vector of the sun in the second equatorial coordinate system $O_s - X_s Y_s Z_s$, S_s , is given by

$$S_s = \begin{bmatrix} \cos \varepsilon \cos \chi \\ \cos \varepsilon \sin \chi \\ \sin \varepsilon \end{bmatrix}, \quad (7)$$

where χ and ε denote the apparent right ascension and declination of the sun, respectively.

Transform S_s from $O_s - X_s Y_s Z_s$ to $O_o - X_o Y_o Z_o$, and the new unit direction vector, S_{o_s} , is expressed as

$$\begin{cases} R_s^o = R_y(-90^\circ - \omega)R_x(i - 90^\circ)R_z(\Omega), \\ S_{o_s} = R_s^o S_s, \end{cases} \quad (8)$$

where ω is the latitude angle, i is the orbital inclination, and Ω is the right ascension of the ascending node; R_x , R_y , and R_z denote the unit rotation matrix around axis x , y , and z , respectively.

The TER pointing mechanism is mounted on the spacecraft, as shown in Figure 11. The unit direction vector of the sun in $O - XYZ$ can be computed as

$$\begin{cases} R_o^d = R_x(-90^\circ)R_y(90^\circ), \\ S_d = R_o^d S_{o_s}. \end{cases} \quad (9)$$

Then, the azimuth angle of the sun ϕ and elevation angle φ in $O - XYZ$ is given by

$$\begin{cases} \phi = \arccos\left(\frac{S_d(x)}{\sqrt{S_d(x)^2 + S_d(y)^2}}\right), \\ \varphi = \arccos\left(\sqrt{S_d(x)^2 + S_d(y)^2}\right). \end{cases} \quad (10)$$

As aforementioned, there are three degrees of freedom in the TER pointing mechanism: two-dimensional rotations, and a translation motion along direction Z . For sun tracking, only the orientation of the mobile platform is required to be determined, which can be done by α and β . The third parameter z is adjustable, which can be used in interesting ways or be optimized as a useful objective function.

Hence, α and β can be given by

$$\begin{cases} \alpha = \phi, \\ \beta = 90^\circ - \varphi, \end{cases} \quad (11)$$

where if $S_d(y) \geq 0$ and $\alpha = -\alpha$.

Substituting equation (11) to equation (6), the length of each extensible rod in the process of sun tracking can be given by

$$l_i = \|L_i\| = \left\| T(\phi, 90^\circ - \varphi, z) \begin{bmatrix} b_i \\ 1 \end{bmatrix} - \begin{bmatrix} a_i \\ 1 \end{bmatrix} \right\|, \quad i = 1, 2, 3. \quad (12)$$

4.3. For Ground Station Communication or Achieving Other Targets. When the TER pointing mechanism drives the CMMR/ECD to face the ground station or achieving other targets, α , β , and δ are can be given as

$$\begin{cases} \alpha = 0^\circ, \\ \beta + \delta = 90^\circ. \end{cases} \quad (13)$$

Then, l_i and δ can be given by

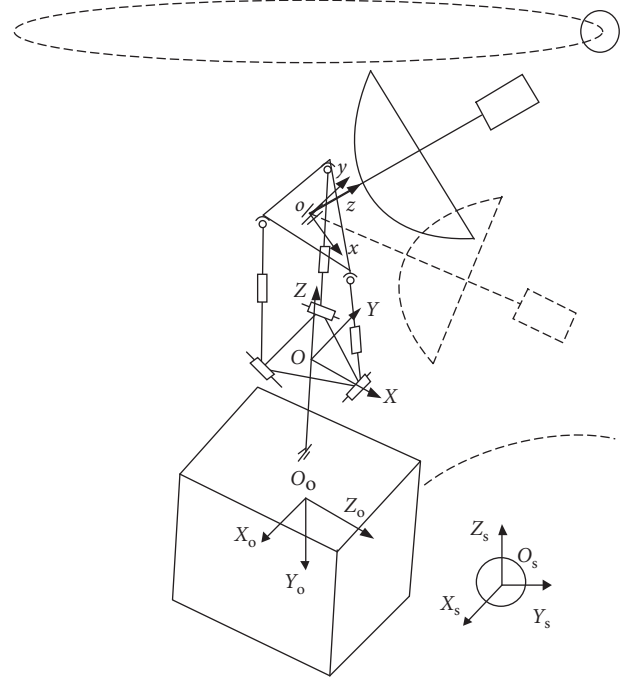


FIGURE 11: Position of the TER pointing mechanism mounting on the spacecraft.

$$\begin{cases} l_i = \left\| T(0, \beta, z) \begin{bmatrix} b_i \\ 1 \end{bmatrix} - \begin{bmatrix} a_i \\ 1 \end{bmatrix} \right\|, \quad i = 1, 2, 3, \\ \delta = 90^\circ - \beta. \end{cases} \quad (14)$$

5. Simulation Analysis of SSPCI

5.1. Parameter Setting. Before the simulation analysis, it is necessary to set related parameters. The spacecraft adopts a hexahedron satellite with dimensions of $2.02 \text{ m} \times 2 \text{ m} \times 2.215 \text{ m}$, and a mass is 985 kg [20]. The orbital parameters are listed in Table 1 [21]. Structural parameters of the CMMR are listed in Table 2, and those of the TER pointing mechanism are shown in Table 3. The energy conversion device is replaced by a cylinder with dimensions of $0.2 \text{ m} \times 0.2 \text{ m}$, and the mass is 3 kg. In the finite element analysis, the rigid structures of the SSPCI use the material of the carbon fiber, the cables use the material of Kevlar, and the reflective membrane uses the material of the aluminized membrane. The properties of the related materials are listed in Table 4. The mass of the CMMR and the ECD is 7.129 kg, the mass of the TER pointing mechanism is 4.3678 kg, and the overall mass of the SSPCI is 11.4968 kg.

5.2. Interference Detection of SSPCI. The relevant dimensions of the system have been given in Section 5.1. However, it should be judged that whether the moving scope of the TER pointing mechanism can satisfy the requirement of the mission, and the SSPCI will interfere with the satellite body in the tracking process.

TABLE 1: Parameters of the orbit.

Orbit parameter	Value
Perigee altitude	825 km
Apogee altitude	827 km
Inclination	98.6551°
RAAN	283.5986°
Argument of perigee	159.3463°
Initial mean anomaly	200.7768°

TABLE 2: Structural parameters of the CMMR and ECD.

Structural parameters	Value
Aperture of the reflector	5 m
Focal/diameter ratio	0.4
Number sections of the deployable hoop	12
Diameter of the hoop bar	6 mm
Thickness of the hoop bar	0.5 mm
Diameter of the central cylinder	50 mm
Thickness of the central cylinder	5 mm
Diameter of the upper/lower support cable	0.3 mm
Diameter of other cables	0.2 mm
Thickness of the aluminized membrane	0.02 mm
Prestrain of the mesh cable	0.0078
Prestrain of the pulling cable	0.0040
Prestrain of the fastening cable	0.0059
Prestrain of the upper support cable	0.0047
Prestrain of the lower support cable	0.0035
Diameter of the feed (instead by the cylinder)	200 mm
Height of the feed (instead by the cylinder)	200 mm

TABLE 3: Structural parameters of the TER pointing mechanism.

Structural parameters	Value
Zero height	600 mm
Diameter of the upper platform	400 mm
Thickness of the upper platform	10 mm
Diameter of the lower platform	200 mm
Thickness of the lower platform	10 mm
Diameter of the upper extensible rod	10 mm
Length of the upper extensible rod	492 mm
Diameter of the lower extensible rod	20 mm
Thickness of the lower extensible rod	5 mm
Length of the lower extensible rod	416 mm
Diameter of the supporting rod	30 mm
Thickness of the supporting rod	5 mm
Length of the supporting rod	693 mm
Working height	700 mm

According to the parameters of the orbit listed in Table 1, through the commercial simulation software, the angle between the sun vector and the orbital plane during one year is plotted in Figure 12. The minimum value of the angle is 18.504°, the maximum value is 29.884°, and the sun vector is always on the one side of the orbital plane. The moving scope of the TER pointing mechanism is mainly limited by the length of each extensible rod and the rotation angles of each compound joint and rotary joint. As listed in Table 3, the minimum length of the extensible rod is 492 mm, and the maximum length is 908 mm. As shown in Figure 8, the

maximum rotation angle of the compound joint is 85°. According to engineering experience, the maximum rotation angle of the rotary joint is 57°. According to literature [22], the moving scope of the TER pointing mechanism is obtained, as shown in Figure 13. The blue part is the workspace of the TER pointing mechanism under the limiting condition, and the orange part is the required workspace for the SSPCI. It can be observed that the moving scope of the TER pointing mechanism can satisfy the requirement of the SSPCI.

In the process of tracking the sun, the most likely time for interference is when the SSPCI turns the diagonal section of the satellite body at the minimum pitch angle, as shown in Figure 14(a). The minimum working height of the supporting structure is calculated as 1393 mm. Because the working height of the TER pointing mechanism is 700 mm, the length of the supporting rod is 693 mm. Figure 14(b) shows the limit position of the SSPCI for communication. It can be observed that the SSPCI will not interfere with the satellite body in the tracking process, thus verifying the correctness of the relevant dimensions.

5.3. Simulation of Deploying Process. The deploying probability is the key performance for a deployable structure. The SSPCI can be deployed by two steps: the deployment of the support structure and the deployment of the folded hoop. The deploying process is simulated by multibody dynamic simulation software.

5.3.1. Support Structure Deployment. The satellite platform is unconstrained in this process. The acceleration of gravity is set to zero. As shown in Figure 15, two rotary drives are applied at the position of motor 1 and motor 2, respectively. The rotation angles of two motors are planned by a cubic polynomial in the deploying process. The relevant settings are made as follows: the deployment time is 200 s; both the angles of the two rotary drives are 90°; both the initial and terminal angular velocities of the two rotary drives are 0°/s. Simulation results show that the support structure can be deployed from status 1 to status 2 successfully, as shown in Figure 15. Dynamic curves of the spacecraft's center of mass with time are shown in Figure 16. The maximum displacement is no more than 15 mm. The maximum velocity and acceleration is no more than 0.35 mm/s and 0.01 mm/s, respectively; the results illustrate that the deployment of the support structure has little effect on the spacecraft. Figure 17 displays the dynamic curves of driving torques of the two motors with time. The maximum of them is not more than 25 Nmm, which indicates that two small and lightweight motors can implement the target.

5.3.2. Folded Hoop Deployment. The deployment of the folded hoop is the second and most important step for the deployment of the SSPCI. The folded hoop is unconstrained in this process. The acceleration of gravity is set to zero. Every two rods are connected by two rotary pairs driven by a torsion spring, which is used to simulate the deployable joint

TABLE 4: Properties of related materials.

	Carbon fiber	Kevlar	Aluminized membrane
Density (kg/m^3)	1.8×10^3	1.45×10^3	1.42×10^3
Young's modulus (Pa)	2.35×10^{11}	1.24×10^{11}	3×10^{11}
Poisson's ratio	0.3	0.3	0.3
Thermal conductivity ($\text{W/m}\cdot^\circ\text{C}$)	400	1	14.4
Coefficient of thermal expansion ($1/^\circ\text{C}$)	2×10^{-6}	-2×10^{-6}	2.5×10^{-5}

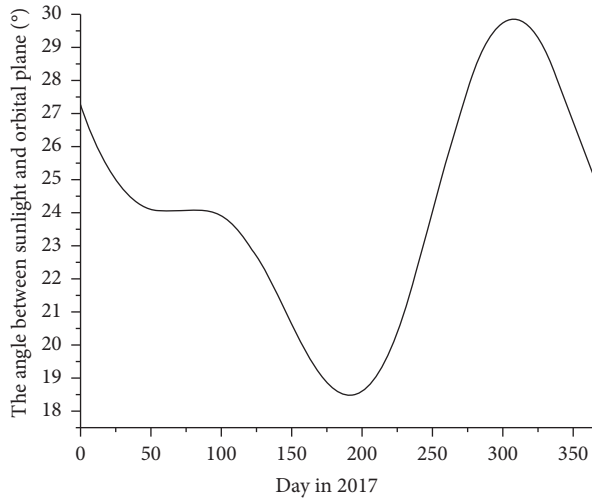


FIGURE 12: Angle between the sun vector and orbital plane.

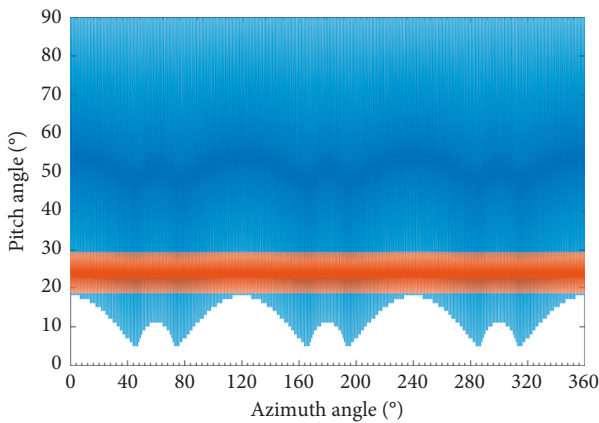


FIGURE 13: Moving scope of the TER pointing mechanism.

introduced in Section 3.1. By controlling the stiffness coefficient and damping coefficient of each rotary pair, the folded hoop is deployed from status 1 to status 2, as shown in Figure 18. Figure 19 shows that the displacement, velocity, and acceleration of the mass center of one of the rotary pairs with time, respectively.

5.4. Static Force Analysis. The SSPCI has to keep a satisfactory mechanical property in space environment. Meanwhile, the CMMR requires a high surface precision for power or communication. Thus, static force analysis of the SSPCI at a limit orientation in zero gravity was carried out.

A simplified $\Phi 5$ m finite element method (FEM) model of the SSPCI was constructed. Parameters of the SSPCI are set based on Section 5.1. BEAM4 is used for the folded hoop, the central cylinder, the TER pointing mechanism, and the supporting rod. LINK10 is used for flexible cables. SHELL41 is used for the aluminized membrane. SOLID45 is used for the ECD and the satellite. The upper end node of each extensible rod and the corresponding position node of the mobile platform are coupled to constrain their three translational degrees of freedom (DOF) to simulate the compound joint. Meanwhile, the lower end node of each extensible rod and the one of the base platform are coupled to constrain their three translation DOF and two rotational DOF to simulate the rotary joint. The bottom of the ECD and the upper end of the central cylinder are rigidly fastened. The Solid45 of the ECD and the spacecraft is generated by mapping mesh into tetrahedron elements, while the other element types are generated by nodes directly. The lower surface of the satellite is fully constrained. The acceleration of gravity is set to zero. Because the main external load of the SSPCI is the temperature load in space, the temperature loads of 20°C , -100°C , and 100°C are applied to the SSPCI, respectively. The large deformation and automatic time step are opened, and the finite element model is analyzed by static force analysis and modal analysis.

Simulation results are shown in Figures 20–23. The maximum displacement of the SSPCI at the temperature load of 20°C is 44 mm, as shown in Figure 20; the RMS of the CMMR is 3.6 mm to the best fit paraboloid after post-treatment, which is small enough to satisfy the requirements of concentrating both sunlight and electromagnetic waves. The fundamental frequency of the SSPCI is 0.9282 Hz, as shown in Figure 21. The fundamental frequency can be increased by further system-level optimization. The maximum displacement of the SSPCI at the temperature load of -100°C is 39 mm, as shown in Figure 22; the RMS of the CMMR is 12 mm. The maximum displacement of the SSPCI at the temperature load of 100°C is 35 mm, as shown in Figure 23; the RMS of the CMMR is 24 mm. Currently, the RMS of the CMMR at the temperature of 100°C is not satisfactory, which can be solved by necessary temperature control measures and further system-level optimization.

5.5. Sun Tracking Process Analysis. As aforementioned, the sun's path can be treated as a circle relative to the spacecraft in one orbital cycle. Therefore, the CMMR/ECD of the SSPCI has to rotate in a circle to follow the sun, which is driven by the TER pointing mechanism. The simulation process in one orbital cycle starting from 0:00 on July 7,

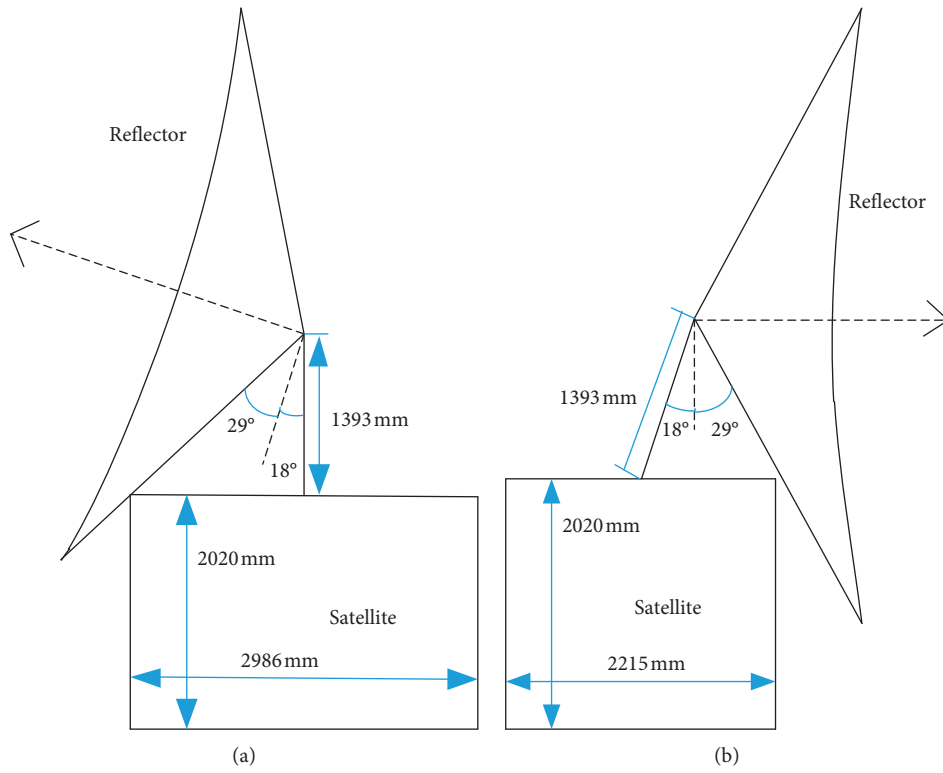


FIGURE 14: Size determination of the support structure: (a) status for power; (b) status for communication.

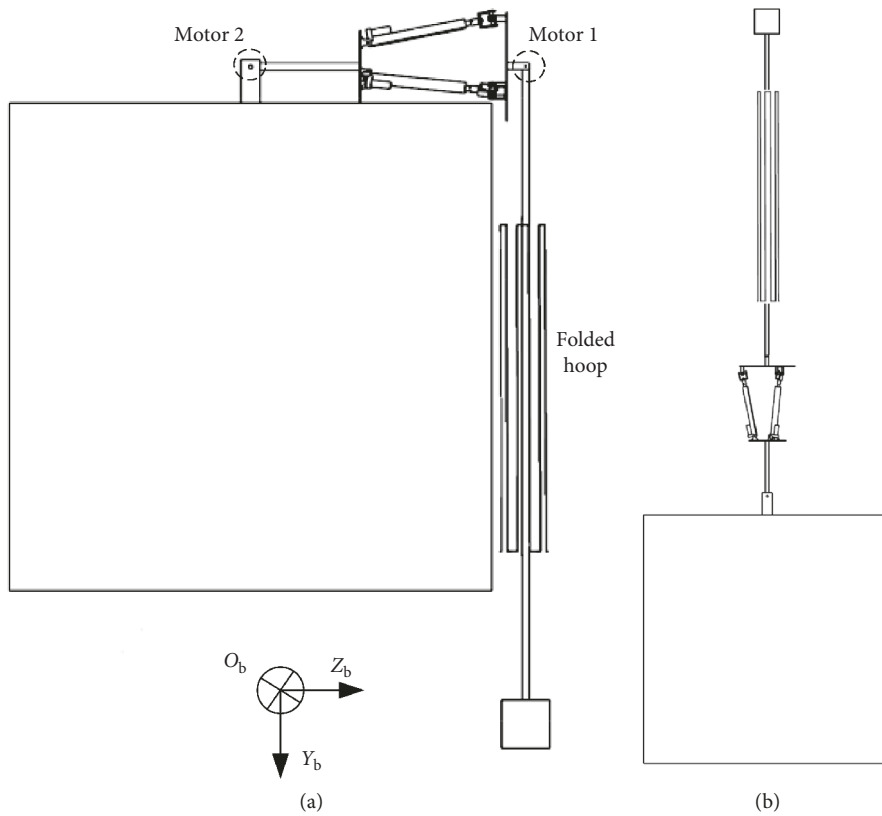


FIGURE 15: Simulation model of the support structure: (a) status 1; (b) status 2.

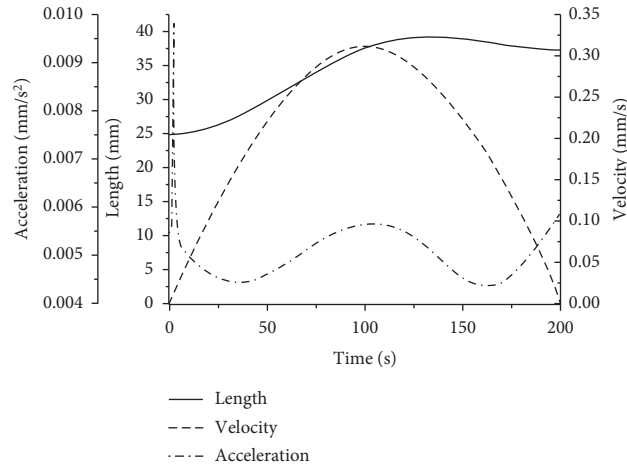


FIGURE 16: Dynamic curves of the spacecraft's center of mass.

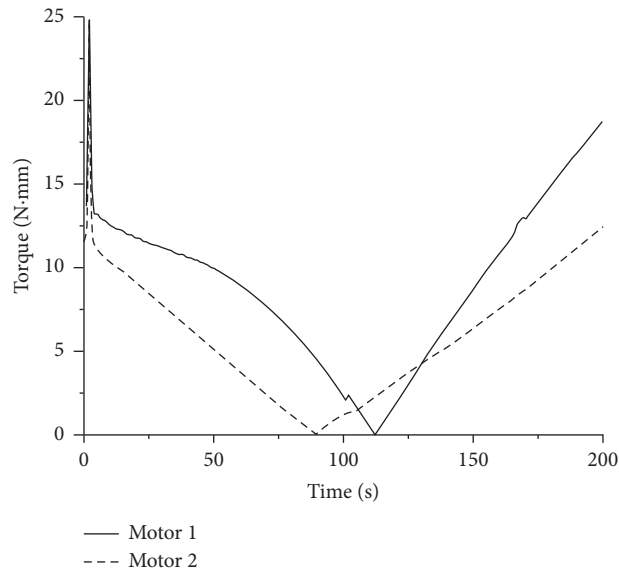


FIGURE 17: Dynamic curves of driving torques of the two motors.

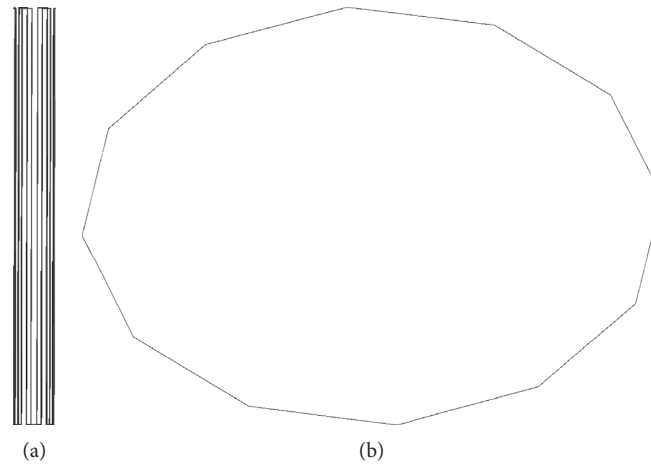


FIGURE 18: Simulation model of the folded hoop deployment: (a) status 1; (b) status 2.

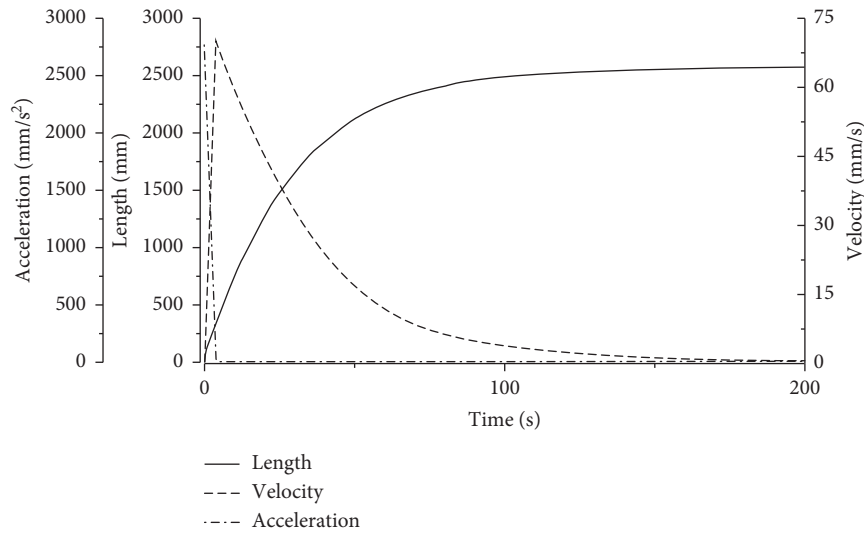


FIGURE 19: Dynamic curves of the mass center of one of the rotary pairs.

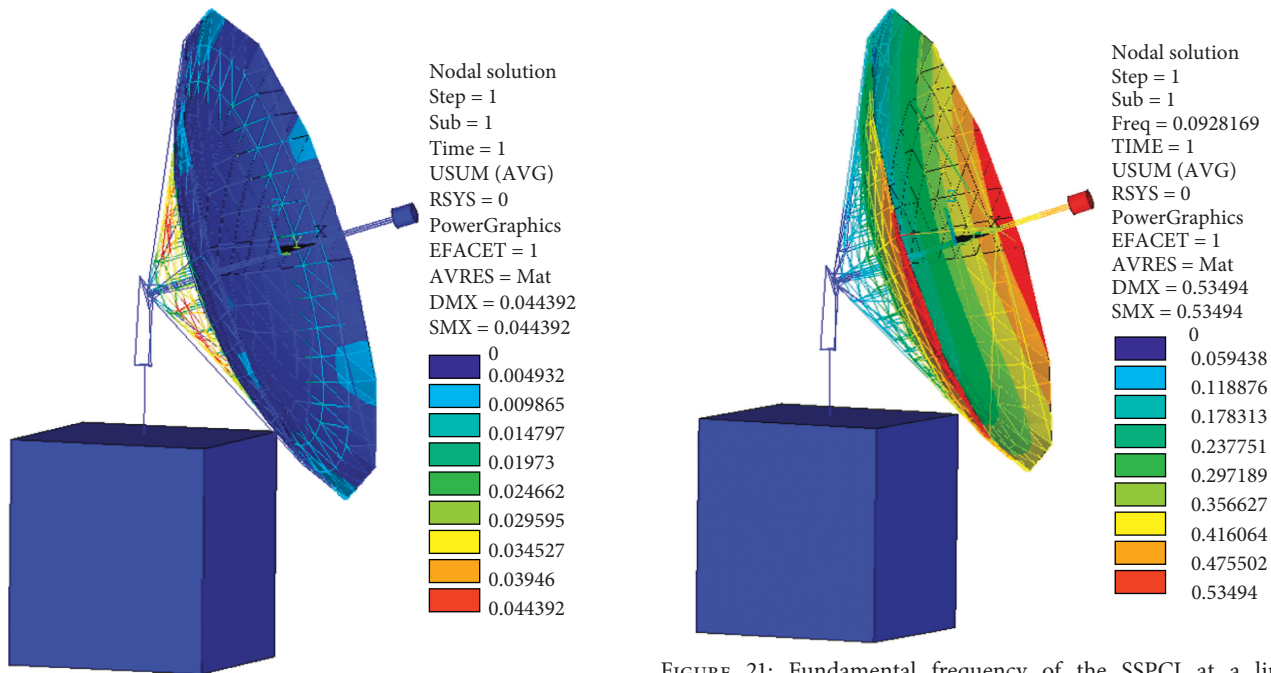


FIGURE 20: Deformation of the SSPCI at a limit orientation under the temperature load of 20°C.

FIGURE 21: Fundamental frequency of the SSPCI at a limit orientation.

2017, is built up. Figure 24 shows the simulation model of the SSPCI. The reflector remains the pitch angle of 18.504° relative to the mounting plane. The velocity of the attitude angle is planned, as shown in Figure 25. Figure 26 displays the dynamic curves of the spacecraft's center of mass with time. The maximum value of displacement, velocity, and acceleration is no more than 20 mm, 0.015 mm/s, and 0.0015 mm/s², respectively; the results illustrates that the motion of the SSPCI has little effect on the spacecraft. Figure 27 displays the dynamic curves of driving forces of three extensible rods with time. The maximum force of each extensible rod is no more than 0.015 N at start up time,

which indicates three low power and lightweight motors can implement the target. Figure 28 displays the dynamic curves of the consumed power of each extensible rod with time from 13 s to 6075 s. Furthermore, the consumed power of three extensible rods in a flying cycle is 2.4186×10^{-4} J. The spacecraft flies 14.2 orbits around the earth in one day. The consumed power of the TER pointing mechanism in one day is 2.9×10^{-3} J, and the consumed power of the TER pointing mechanism in one year with 365 days is 1.06 J. Figure 29 displays the dynamic curves of the distance between the upper and lower U plates of each compound joint with time. It can be observed that the distance of each compound joint is always greater than zero; the results illustrate that there is

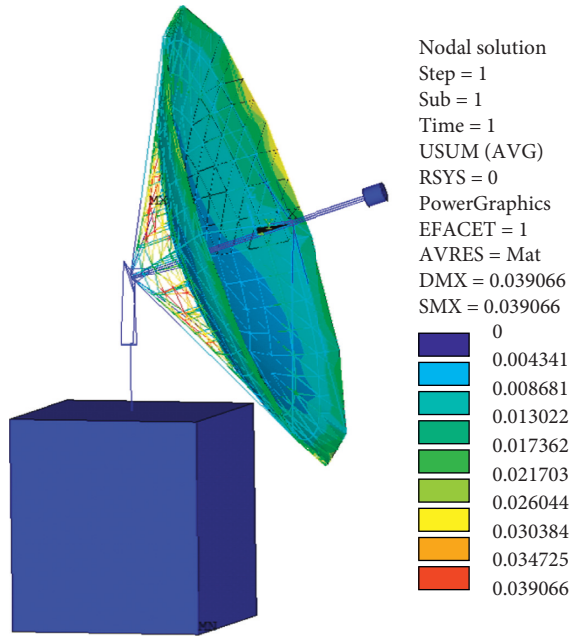


FIGURE 22: Deformation of the SSPCI at a limit orientation under the temperature load of -100°C .

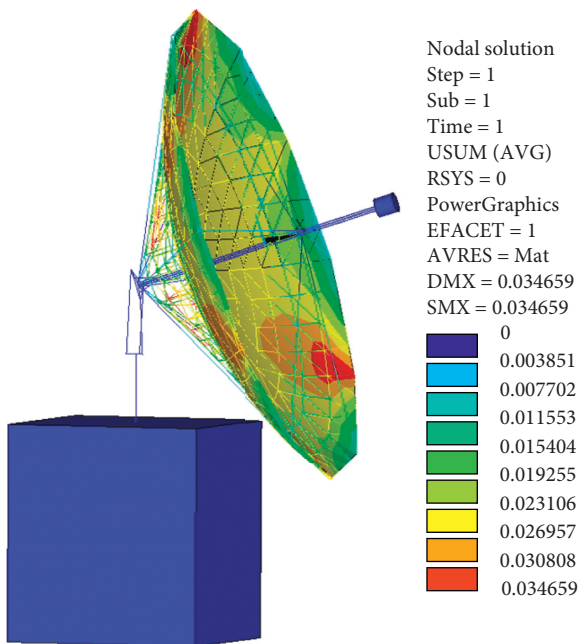


FIGURE 23: Deformation of the SSPCI at a limit orientation under the temperature load of 100°C .

no interference between the upper and lower U plates, and the design of the compound joint is feasible, stability, and reliability for the SSPCI.

6. Key Experiments for SSPCI on the Ground

6.1. *Deployment Experiments of Folded Hoop on the Ground.* The deploying probability of the folded hoop is the key technology for the SSPCI. As limitation of experimental

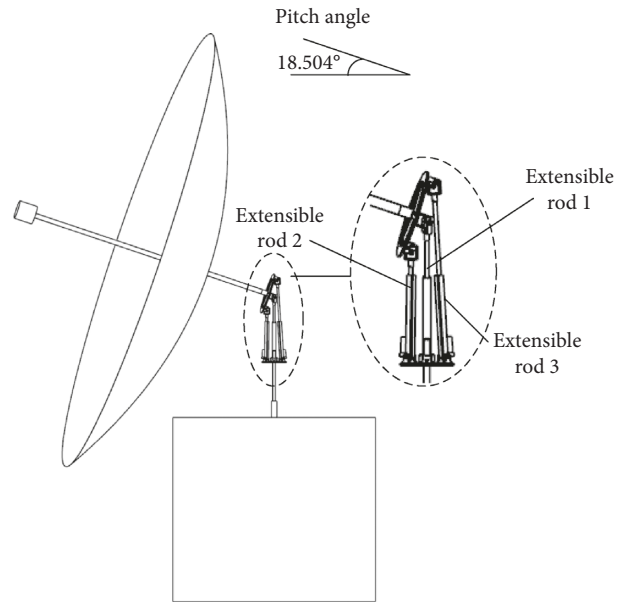


FIGURE 24: Simulation model of the sun tracking process.

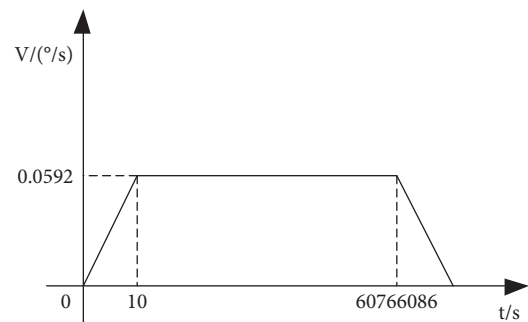


FIGURE 25: Planned velocity of the attitude angle.

conditions, an actual and scale $\Phi 2\text{ m}$ model was designed to test the deploying dependability of the folded hoop.

The folded hoop is constructed with 36 aluminum bars, whose outer diameter is $\Phi 1\text{ mm}$ and thickness is 0.2 mm . The stowed size of the folded hoop is $\Phi 17\text{ mm} \times 19\text{ mm}$. The actual model is hung to compensate the gravity influence, as shown in Figure 30(a). After releasing the rubber hand, the model can be deployed successfully as similar as the simulation analysis. Figure 30(b) shows the deployed status of the actual model.

Due to the parallel driving manner of the torsion spring, although the actual model is not precisely manufactured and assembled, it can still be deployed successfully. This illustrates that the structure has a fairly high deploying dependability.

6.2. *Sun Tracking Experiments of TER Pointing Mechanism on the Ground.* Although theoretical and simulation analysis of the TER pointing mechanism have been made, it is still doubtful for its feasibility without an actual test. Thus, we have carried out sun tracking experiments of the TER pointing mechanism on the ground successfully. Although

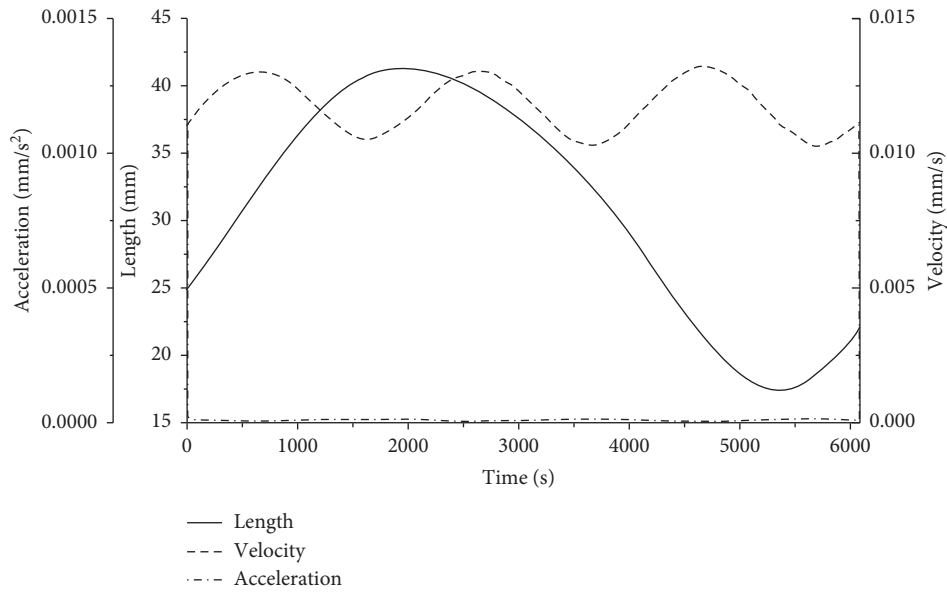


FIGURE 26: Dynamic curves of the spacecraft's center of mass.

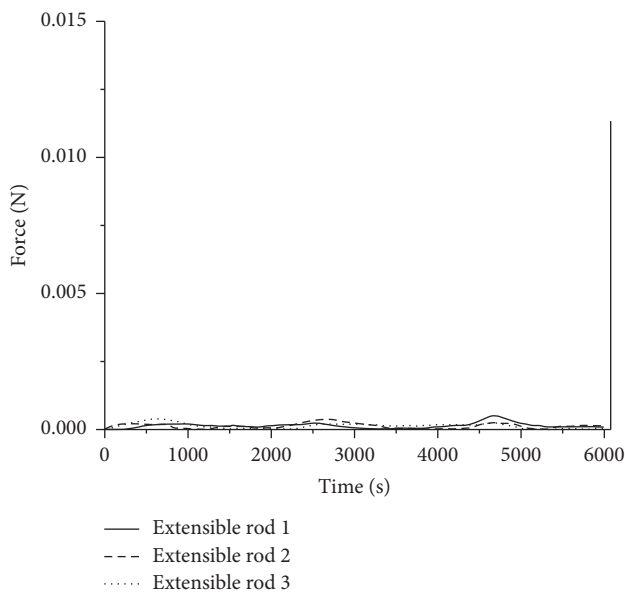


FIGURE 27: Driving forces of the three extensible rods with time.

the environment on the ground is different from the one in space, and the mechanism principle and control mode of the TER pointing mechanism are identical. Therefore, it can be indirectly predicted that the TER pointing mechanism is feasible for the SSPCI in a space environment. Figure 31 shows three moments of the sun tracking process in a day. Although the precision of manufacture is not high, it can still be observed that the central cylinder has no projection on the mobile platform at the three moments (morning moment in Figure 31(a), noon moment in Figure 31(b), and afternoon moment in Figure 31(c)). The shadow region on the mounting sleeve on the morning moment is shown in Figure 31(d). The wall thickness of the mounting sleeve is 6 mm, and the length of the central cylinder is 895 mm. This

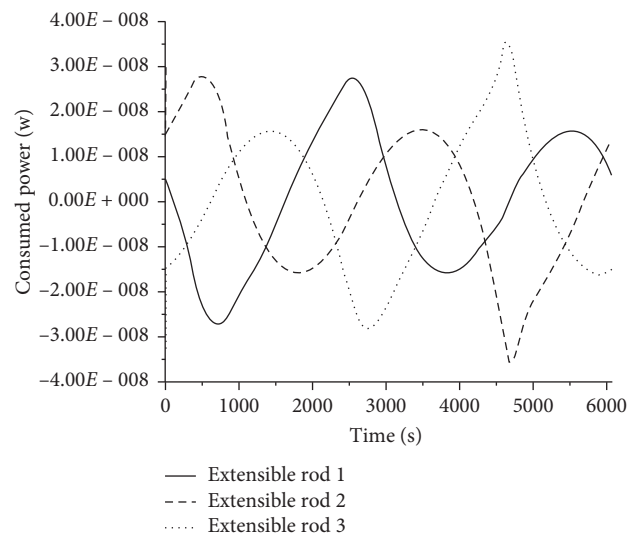


FIGURE 28: Consumed power of each extensible rod with time.

illustrates that the tracking precision of the TER pointing mechanism is within 0.4° (i.e., $\arctan(6/895)$), which is sufficient for the SSPCI.

7. Conclusions

A novel SSPCI is designed in this paper. The theoretical analysis, simulation analysis, and preliminary experiments on the ground are conducted for the SSPCI. Analytical deduction and experiments show that the SSPCI has several remarkable advantages, which can be summarized as follows:

- (1) Due to integrating two functions (for power and communication) on one paraboloid structure, a large-size solar array and a large-size communication antenna can be combined into one.

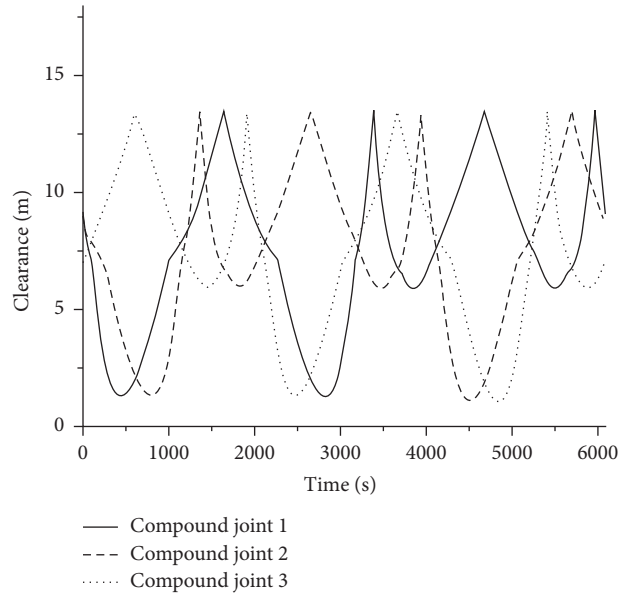


FIGURE 29: Distance between upper and lower U plate of each compound joint with time.

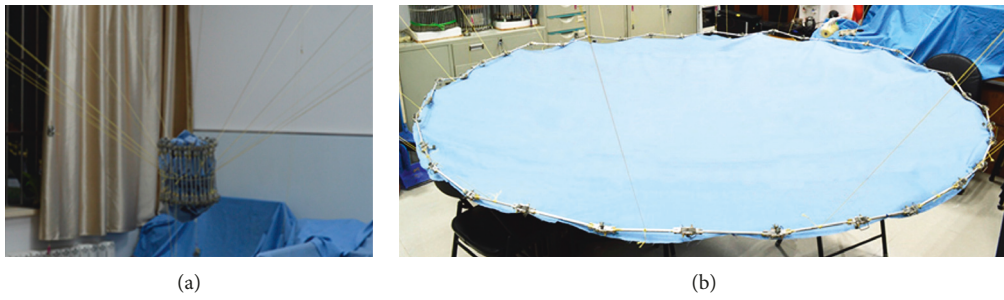


FIGURE 30: Deployment experiments of the folded hoop on the ground: (a) stowed status; (b) deployed status.

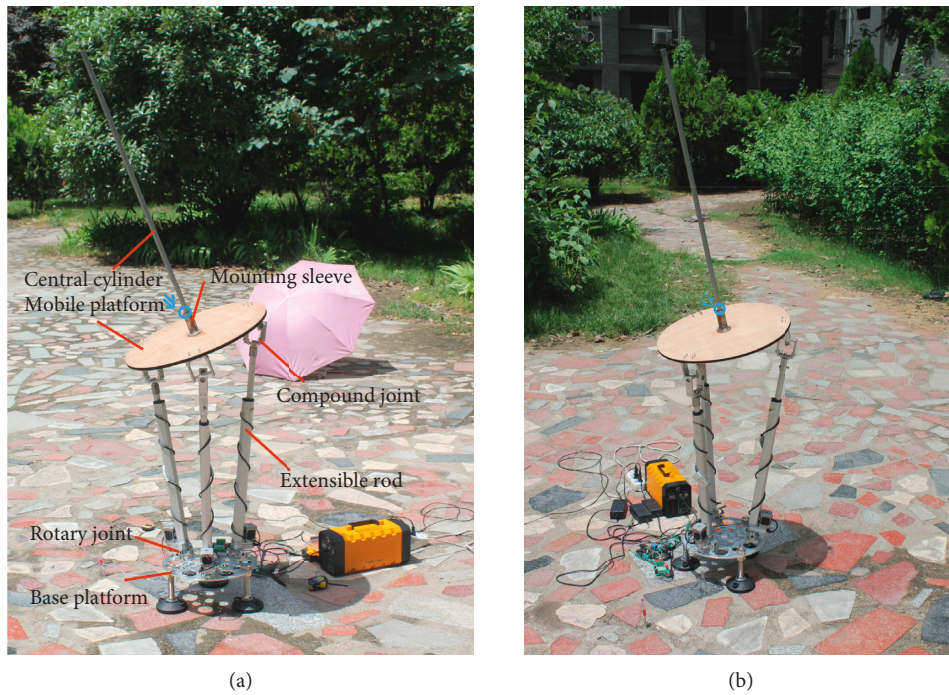


FIGURE 31: Continued.



(c)



(d)

FIGURE 31: Three moments of the sun tracking process of the TER pointing mechanism on the ground: (a) morning moment; (b) noon moment; (c) afternoon moment. (d) The shadow region on the mounting sleeve.

TABLE 5: Predicted comparison between the SSPCI and the solar panel.

Structure type	Solar panel	SSPCI (5 m)
Size (m)	$1.530 \times 2 \times 0.025$	5
Conversion efficiency (%)	27	30 (predicted)
Surface density (kg/m^2)	2.953	0.5817
Power density (W/kg)	125	502

- (2) The SSPCI is an ultralight paraboloid structure. Compared with the solar panel [23], the surface density of SSPCI is lower, while its power density is higher, as listed in Table 5.
- (3) Although only the SSPCI with an aperture of $\Phi 5$ m is simulated and analyzed, its aperture may be further expanded to $\Phi 20$ m to meet the requirements of a higher power spacecraft because of its low surface density.
- (4) The novel TER pointing mechanism with simple structure, lightweight, and high pointing accuracy can be used for many other applications in space environment.

One of the major area of focus for future works would be the optimal design of the size and shape of the SSPCI in a specific orbit for a given power supply and communication rate required by a specific satellite. In addition, the stability and reliability of the SSPCI should be analyzed in more detail according to the space environment.

Data Availability

The data used to support the finding the study are available from the corresponding author upon request.

Conflicts of Interest

The authors declare that there are no conflicts of interest regarding the publication of this paper.

Acknowledgments

This work was partially supported by the National Natural Science Foundation of China (no. 50975217).

References

- [1] A. H. Lokman, P. J. Soh, S. N. Azemi et al., "A review of antennas for picosatellite applications," *International Journal of Antennas and Propagation*, vol. 2017, p. 17, 2017.
- [2] J. Huang and M. Zawadzki, "Antennas integrated with solar arrays for space vehicle applications," in *Proceedings of the 5th International Symposium on Antennas, Propagation and EM Theory ISAPE 2000*, pp. 86–89, IEEE, Beijing, China, August 2000.
- [3] S. Vaccaro, J. R. Mosig, and P. de Maagt, "Two advanced solar antenna "SOLANT" designs for satellite and terrestrial communications," *IEEE Transactions on Antennas and Propagation*, vol. 51, no. 8, pp. 2028–2034, 2003.
- [4] T. W. Turpin and R. Baktur, "Meshed patch antennas integrated on solar cells," *IEEE Antennas and Wireless Propagation Letters*, vol. 8, pp. 693–696, 2009.
- [5] O. O'Conchubhair, P. McEvoy, and M. J. Ammann, "Integration of inverted-F antenna with solar cell substitute," in *Proceedings of the 2012 loughborough antennas & propagation conference (LAPC)*, pp. 1–4, IEEE, Loughborough, UK, November 2012.
- [6] W. An, S. Xu, F. Yang, and J. Gao, "A ka-band reflectarray antenna integrated with solar cells," *IEEE Transactions on Antennas and Propagation*, vol. 62, no. 11, pp. 5539–5546, 2014.
- [7] S. Vaccaro, P. Torres, J. R. Mosig et al., "Integrated solar panel antennas," *Electronics Letters*, vol. 36, no. 5, pp. 390–391, 2000.

- [8] J. Huang, "Capabilities of printed reflectarray antennas," in *Proceedings of the International Symposium on Phased Array Systems and Technology*, pp. 131–134, IEEE, Boston, MA, USA, October 1996.
- [9] A. Holland, W. Lysford, J. Pearson et al., "Origami style solar panels with development of dual purpose integrated phased array communications system," in *University of North Dakota's Forum 2016*, BerkeleyElectronic Press, Berkeley, CA, USA, 2016.
- [10] D. Lichodziejewski and C. Cassapakis, "Inflatable power antenna technology," in *Proceedings of the 37th Aerospace Sciences Meeting and Exhibit*, p. 1074, Reno, NV, USA, January 1999.
- [11] F. Zheng, M. Chen, and P. Li, "Structural-electromagnetic performance prediction of a new large deployable space antenna," in *Proceedings of the 2010 Aerospace Conference*, pp. 1–7, IEEE, Big Sky, MT, USA, April 2010.
- [12] F. Zheng, M. Chen, and J. He, "Analyses of a new simplified large deployable reflector structure," in *Proceedings of the 2013 Aerospace Conference*, pp. 1–7, IEEE, Big Sky, MT, USA, March 2013.
- [13] F. Zheng and M. Chen, "New conceptual structure design for affordable space large deployable antenna," *IEEE Transactions on Antennas and Propagation*, vol. 63, no. 4, pp. 1351–1358, 2015.
- [14] F. Zheng, X. Rui, and M. Chen, "A rotary thermal-electric conversion device adopting circulating phase change cavity," Chinese Patent No. 201711144633.X, 2017.
- [15] Z. Huang and D. X. Zeng, *Calculation Principle and Method of Freedom of Mechanism*, pp. 153–156, Higher Education Press, Beijing, China, 2016.
- [16] X. Wu, Y. Lu, X. Duan, D. Zhang, and W. Deng, "Design and DOF analysis of a novel compliant parallel mechanism for large load," *Sensors*, vol. 19, no. 4, p. 828, 2019.
- [17] F. Zheng, M. Chen, W. Li, and P. Yang, "Conceptual design of a new huge deployable antenna structure for space application," in *Proceedings of the 2008 IEEE Aerospace Conference*, pp. 1–7, IEEE, Big Sky, MT, USA, March 2008.
- [18] J. Meeus, *Astronomical Algorithms*, pp. 151–157, Willmann-Bell Inc, Richmond, VA, USA, 1998.
- [19] T. Zheng, F. Zheng, X. Rui et al., "A precise algorithm for computing sun position on a satellite," *Journal of Aerospace Technology and Management*, vol. 11, 2019.
- [20] S. Z. Wang, G. W. Zhu, W. H. Bai et al., "For the first time fengyun3 C satellite-global navigation satellite system occultation sounder achieved spaceborne Bei Dou system radio occultation," *Acta Physica Sinica*, vol. 64, no. 8, pp. 89301–089301, 2015.
- [21] HEAVENS ABOVE, FENGYUN 3D [DB/OL], <https://www.heavensabove.com/orbit.aspx?satid=43010&lat=0&lng=0&loc=Unspecified&alt=0&tz=UCT,1994-2-8/2017-12-9>.
- [22] Y. Lu and Y. Zhao, "Position and workspace analyses of 3-SPR and 3-RPS parallel manipulators," in *Proceedings of the ASME 2005 International Design Engineering Technical Conferences and Computers and Information in Engineering Conference*, pp. 957–962, American Society of Mechanical Engineers Digital Collection, Long Beach, CA, USA, September 2005.
- [23] L. C. Duan, H. Q. Li, X. F. Liu, and G. P. Cai, "Rigid-flexible coupling dynamics and control of solar arrays," *Journal of Vibration Engineering*, vol. 28, no. 5, pp. 770–777, 2015.



Hindawi

Submit your manuscripts at
www.hindawi.com

